


RESEARCH PAPER



## RAB21 controls autophagy and cellular energy homeostasis by regulating retromer-mediated recycling of SLC2A1/GLUT1

Yifei Pei<sup>a\*</sup>, Shuning Lv<sup>a\*</sup>, Yong Shi<sup>a</sup>, Jingwen Jia<sup>a</sup>, Mengru Ma<sup>a</sup>, Hailong Han<sup>b</sup>, Rongying Zhang<sup>a</sup>, Jieqiong Tan<sup>c</sup>, and Xinjun Zhang <sup>a</sup>

<sup>a</sup>Key Laboratory of Molecular Biophysics of the Ministry of Education, College of Life Science and Technology, Huazhong University of Science and Technology, Wuhan, China; <sup>b</sup>Department of Neuroscience, Postdoctoral Station for Basic Medicine, Hengyang School of Medicine, University of South China, Hengyang, China; <sup>c</sup>Centre for Medical Genetics and Hunan Key Laboratory of Medical Genetics, School of Life Sciences, Central South University, Changsha, China

### ABSTRACT

The endosomal system maintains cellular homeostasis by coordinating multiple vesicular trafficking events, and the retromer complex plays a critical role in endosomal cargo recognition and sorting. Here, we demonstrate an essential role for the small GTPase RAB21 in regulating retromer-mediated recycling of the glucose transporter SLC2A1/GLUT1 and macroautophagy/autophagy. RAB21 depletion mis-sorts SLC2A1 to lysosomes and affects glucose uptake, thereby activating the AMPK-ULK1 pathway to increase autophagic flux. RAB21 depletion also increases lysosome function. Notably, RAB21 depletion does not overtly affect retrograde transport of IGF2R/CI-M6PR or WLS from endosomes to the trans-Golgi network. We speculate that RAB21 regulates fission of retromer-decorated endosomal tubules, as RAB21 depletion causes accumulation of the SNX27-containing retromer complex on enlarged endosomes at the perinuclear region. Functionally, RAB21 depletion sensitizes cancer cells to energy stress and inhibits tumor growth *in vivo*, suggesting an oncogenic role for RAB21. Overall, our study illuminates the role of RAB21 in regulating endosomal dynamics and maintaining cellular energy homeostasis and suggests RAB21 as a potential metabolic target for cancer therapy.

### ARTICLE HISTORY

Received 17 March 2022  
Revised 8 August 2022  
Accepted 15 August 2022

### KEYWORDS



Autophagic flux; glucose uptake; membrane trafficking; retromer complex; small GTPases

### Introduction


Macroautophagy (hereafter referred to as autophagy) is an evolutionarily conserved lysosomal degradative pathway by which intracellular constituents, organelles and pathogens are recycled or removed [1]. Basal autophagy maintains cellular homeostasis by removing protein aggregates and damaged organelles, and autophagic flux is rapidly enhanced under stress conditions to produce necessary nutrients and energy for cell survival [2]. The autophagic flux process is composed of the initiation of phagophores, phagophore expansion and sequestration of proteins and organelles, autophagosome maturation and fusion with lysosomes, and cargo degradation [3]. This process is governed by a series of autophagy-related proteins and has been extensively studied. AMP-activated protein kinase (AMPK) and mechanistic target of rapamycin kinase (MTOR) complex 1 (MTORC1) are two major upstream regulators of autophagy that control autophagy by differentially phosphorylating ULK1 (unc-51 like autophagy activating kinase 1), the key kinase for autophagy initiation [4–9]. AMPK is a major energy sensor and regulator that phosphorylates ULK1 to enhance its activity and thus activate autophagy, while MTORC1 phosphorylates

ULK1 at different residues to inhibit ULK1 activity and autophagy.

The retromer complex plays central roles in coordinating endosomal dynamics by sorting cargos from endosomes to the trans-Golgi network (TGN) or to the plasma membrane [10–12]. The core complex of the retromer consists of VPS35, VPS29 and VPS26, which form a stable trimer and associate with a series of other proteins to generate endosomal tubular-vesicular carriers [13]. The cargo specificity is determined by retromer core complex association with different SNX (sorting nexin) proteins [10,11]. The SNX27-associated retromer governs transportation from endosomes to the plasma membrane, and one of the typical cargos is SLC2A1/GLUT1, while the SNX3-associated retromer controls transportation from endosomes to the TGN, and IGF2R/CI-M6PR (insulin like growth factor 2 receptor) is one of the typical cargos. Glucose is the main energy source for the majority of cells, and SLC2A1 is one of the best characterized glucose transporters that is ubiquitously expressed and mediates basal glucose uptake in most cell lines [14]. IGF2R is a major transporter of lysosome hydrolases and shuttles between the TGN and endosomes to deliver newly synthesized hydrolases, such as CTSB (cathepsin B), to the endolysosomal system [15]. Thus,

**CONTACT** Xinjun Zhang  [xinjunzhang@hust.edu.cn](mailto:xinjunzhang@hust.edu.cn)  Key Laboratory of Molecular Biophysics of the Ministry of Education, College of Life Science and Technology, Huazhong University of Science and Technology, Luoyu Road 1037, Wuhan, Hubei 430074, China

\*These authors contributed equally to this work.

 Supplemental data for this article can be accessed online at <https://doi.org/10.1080/15548627.2022.2114271>

© 2022 Informa UK Limited, trading as Taylor & Francis Group

retromer function is critical for cellular energy homeostasis and lysosome activity and is closely related to autophagy.

RAB21 belongs to the RAB5 subfamily of small GTPases, which mainly regulate endocytosis [16,17]. Early studies showed that RAB21 is localized on early endosomes and may regulate endosomal dynamics and internalization of transferrin and epidermal growth factor [17–19]. A series of studies revealed that RAB21 directly interacts with several integrins and regulates integrin endocytosis and integrin-related functions such as cytokinesis [20–22]. Conversely, recent studies have connected RAB21 to autophagy and the retromer [23,24]. However, how RAB21 regulates autophagy and retromer function remains elusive.

In the present study, we reexamined the function of RAB21 using the CRISPR-Cas9-mediated knockout approach. In contrast to previous studies [23,24], we show that RAB21 depletion increases autophagic flux by activating the AMPK-ULK1 axis and increasing lysosome activity. We further demonstrate that RAB21 regulates retromer-mediated recycling of SLC2A1 from endosomes to the plasma membrane and maintains cellular energy homeostasis. Furthermore, RAB21 depletion sensitizes cancer cells to energy stress and inhibits tumor growth in vivo, suggesting that RAB21 is a potential target for cancer therapy.

## Results

### **RAB21 regulates basal and starvation-induced autophagic flux**

In the process of characterizing the phenotypes of *RAB21* knockout (*RAB21* KO) HeLa cells, we observed that the levels of LC3-II, a typical autophagosome marker [3], were increased in *RAB21* KO cells constructed by two independent sgRNAs via the CRISPR-Cas9 approach under both basal and starvation conditions (Figure 1A–B). We further applied two lysosomal inhibitors, bafilomycin A<sub>1</sub> (Baf.A<sub>1</sub>) and chloroquine (CQ) to monitor autophagic flux [3,25]. In the presence of Baf.A<sub>1</sub>, the levels of LC3-II in *RAB21* KO cells were further increased and significantly higher than those in wild-type (WT) cells under both basal and starvation conditions (Figure 1C–D), confirming the elevation of autophagic flux. Meanwhile, re-expressing GFP-RAB21 in *RAB21* KO cells rescued the elevated autophagic flux (Figure 1C–D). On the other hand, overexpressing GFP-RAB21 decreased, while overexpressing GFP-RAB21<sup>T33N</sup>, a dominant-negative form, increased, the autophagic flux in WT HeLa cells, further suggesting that RAB21 inhibits autophagic flux (Figure 1E–H). We next performed immunostaining experiments to visualize endogenous LC3. As shown in Figure 1I–J, more LC3 puncta were observed in *RAB21* KO cells under basal and starvation conditions with or without Baf.A<sub>1</sub> treatment, consistent with the results in Figure 1C–D.

To monitor autophagosome maturation, the tandem mCherry-GFP-LC3 reporter was expressed in both WT and *RAB21* KO cells. This GFP fluorescence is pH sensitive and would be quenched in acidic compartments, so mCherry and GFP double-positive (mCherry+ GFP+) vesicles label immature autophagosomes, while mCherry-positive but GFP-

negative (mCherry+ GFP-) vesicles are acidified autolysosomes [26]. Compared to WT cells, the percentage of mCherry+ GFP- structures was significantly increased in *RAB21* KO cells under both basal and starvation conditions (Figure 1K–L), suggesting that the autophagosome clearance efficiency is elevated in *RAB21* KO cells.

Additionally, *RAB21* KO in two other cell lines, U2OS and 293A, also caused elevated autophagic flux under both basal and starvation conditions, suggesting that RAB21 negatively regulating autophagy is not cell type specific (Figure 1M–N).

### **RAB21 KO cells are more sensitive to energy stress but resistant to ferroptosis induced by erastin**

As RAB21 regulates autophagy, we wondered whether RAB21 contacts autophagic structures directly. We performed immunostaining in HeLa cells stably expressing GFP-RAB21 to visualize the cellular localization of RAB21. The results showed that RAB21 colocalized well with the early endosome marker EEA1 (Fig. S1A and S1D), consistent with previous studies [17,19]. However, we did not observe overt colocalization between RAB21 and either the autophagosome marker LC3 or the lysosome marker LAMP1 (Fig. S1B–D), implying that RAB21 may regulate autophagy indirectly.

Autophagy is crucial for maintaining a basic cellular supply of nutrition and energy, and cells use autophagy as a survival strategy to counteract stresses. We next evaluated the effect of *RAB21* KO on the cell response to different stresses. We cultured WT and *RAB21* KO HeLa cells in glucose-free (–Glc.), low-glucose (1 mM Glc.) or serum-free (–FBS) media to observe cell survival. The results showed that *RAB21* KO cells were more sensitive to these stresses, and at the indicated time points, the death rates and the apoptosis rates of *RAB21* KO cells were both significantly higher than those of WT cells (Figure 2A–O and Fig. S1E). In addition, *RAB21* KO cells were also more sensitive to amino acid starvation (Fig. S1F).

As the relationship between autophagy and ferroptosis is intricate [27–29], we also examined the cell response to the ferroptosis inducer erastin (Era.). To our surprise, *RAB21* KO 293A cells were more resistant to Era. than WT cells (Fig. S1 G). As further confirmation, ferrostatin-1 was used to inhibit the ferroptosis induced by Era. (Fig. S1 G). A similar phenomenon was observed in *RAB21* KO HeLa cells (Fig. S1 H–I). We therefore concluded that *RAB21* KO cells were more sensitive to energy stresses and resistant to ferroptosis.

### **RAB21 KO activates the AMPK-ULK1 pathway**

The response of *RAB21* KO cells to energy stresses implies that these cells might suffer from crisis under normal culture conditions and that the elevated autophagic flux might be a compensatory effect. Thus, the activities of the two major upstream regulators of autophagy, AMPK and MTORC1, were examined. The results showed that *RAB21* KO did not affect MTORC1 activity, as indicated by the phosphorylation (p-) of RPS6 (ribosomal protein S6) (Figures 3A–B and 3E). Interestingly, we observed clear elevations in AMPK activity in *RAB21* KO cells, as shown by the increases in PRKAA/

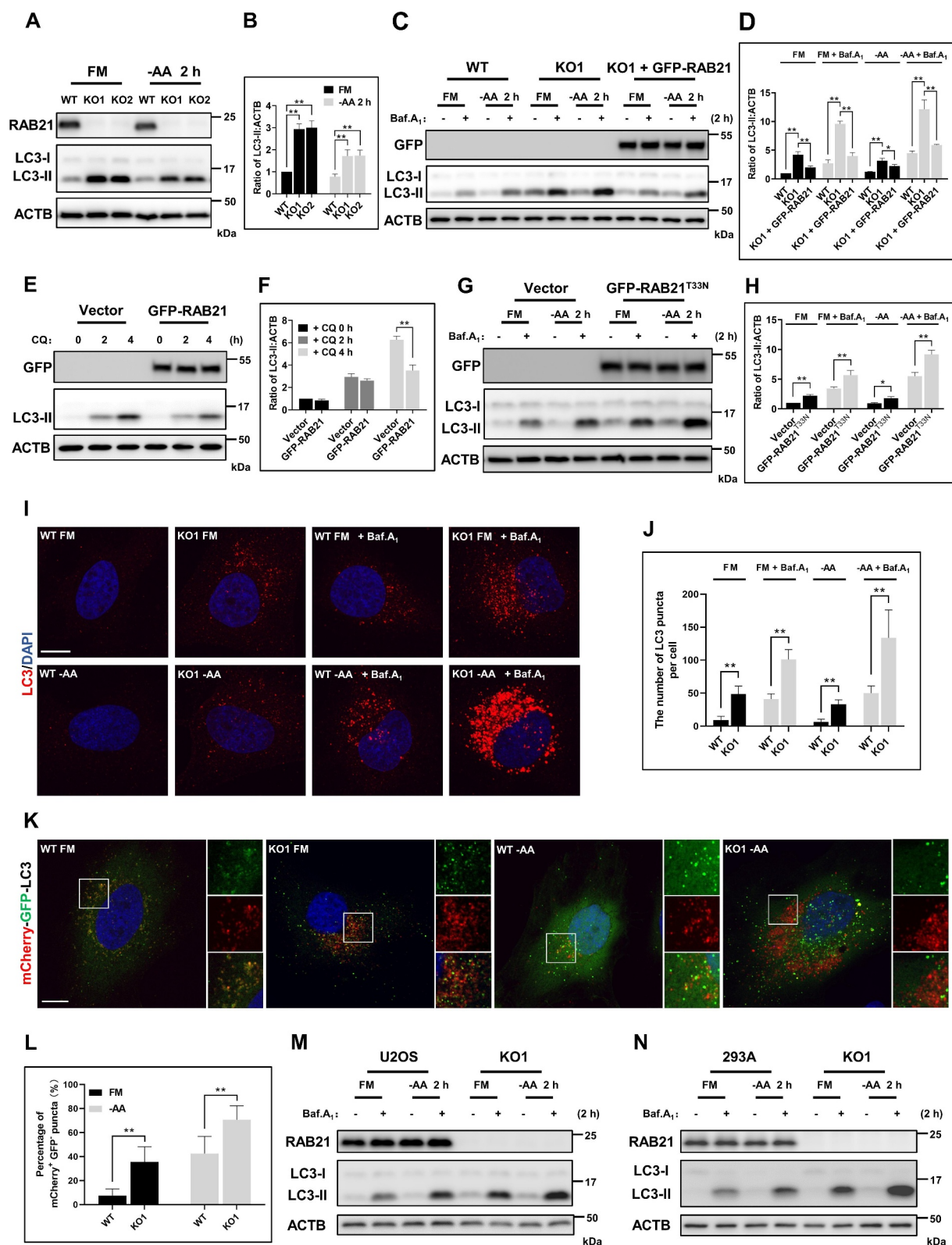


**Figure 1.** RAB21 regulates basal and starvation-induced autophagic flux. (A–B) WT and *RAB21* KO HeLa cells were cultured in full medium (FM) or amino acid-free medium (–AA). The levels of LC3 were examined, and the quantitative results from three independent experiments are shown in B. (C–D) WT, *RAB21* KO, and *RAB21* KO re-expressing GFP-*RAB21* HeLa cells were cultured in FM or –AA with or without 100 nM bafilomycin A<sub>1</sub> (Baf.A<sub>1</sub>). The LC3 levels were examined, and the quantitative results from three independent experiments are shown in D. (E–F) WT and GFP-*RAB21*-expressing HeLa cells were cultured in FM with or without 50  $\mu$ M chloroquine (CQ). The LC3 levels were examined, and the quantitative results from three independent experiments are shown in F. (G–H) WT and GFP-*RAB21*<sup>T33N</sup>-expressing HeLa cells were cultured in FM or –AA with or without 100 nM Baf.A<sub>1</sub>, the LC3 levels were examined, and the quantitative results from three independent experiments are shown in H. (I–J) WT and *RAB21* KO HeLa cells were cultured in FM or –AA, with or without 100 nM Baf.A<sub>1</sub>, and LC3 puncta were detected by immunostaining. Scale bar: 10  $\mu$ m. Quantitative results are shown in J.  $n > 30$  cells from three independent experiments. (K–L) mCherry-GFP-LC3 was expressed in both WT and *RAB21* KO HeLa cells cultured in FM or –AA. LC3 puncta were monitored, and the percentage of mCherry+ GFP+ puncta (autolysosomes) was quantified in L ( $n > 35$  cells from three independent experiments). Scale bar: 10  $\mu$ m. (M) WT and *RAB21* KO U2OS cells were cultured in FM or –AA with or without 100 nM Baf.A<sub>1</sub>. (N) WT and *RAB21* KO 293A cells were cultured in FM or –AA with or without 100 nM Baf.A<sub>1</sub>. The graphs express the mean  $\pm$  SEM. \* $P < 0.05$ ; \*\* $P < 0.01$ ; NS, not significant.



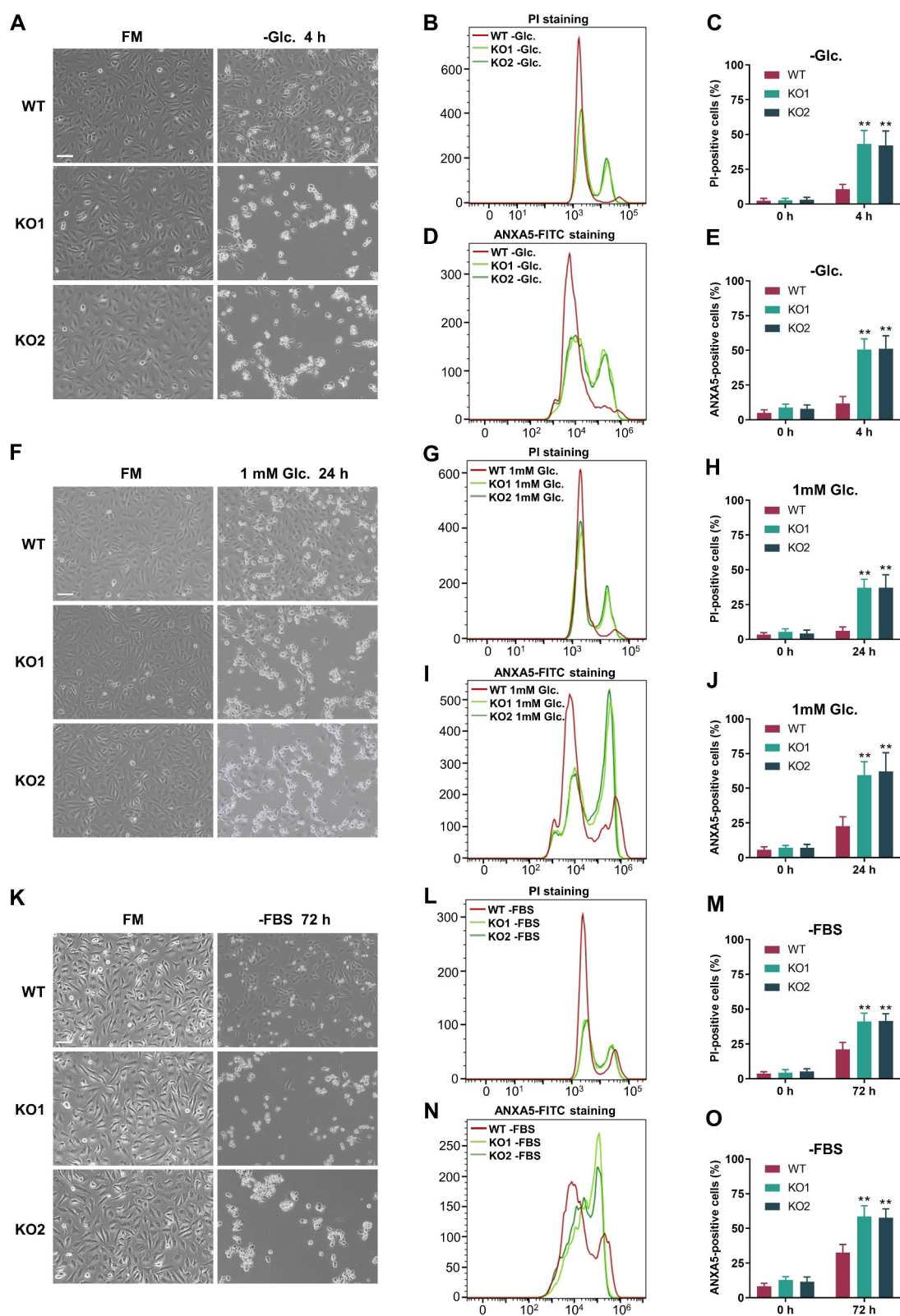


**Figure 2.** *RAB21* KO cells are more sensitive to energy stress. (A-E) WT and *RAB21* KO HeLa cells were cultured in FM or glucose-free (-Glc.) medium. (F-J) WT and *RAB21* KO HeLa cells were cultured in FM or low glucose (1 mM) medium. (K-O) WT and *RAB21* KO HeLa cells were cultured in serum-free (-FBS) medium. Representative images are shown. Cell death was quantified by flow cytometry through PI or ANXA5-FITC staining, and the results from three independent experiments were statistically analyzed. Scale bars: 100  $\mu$ m. The graphs express the mean  $\pm$  SEM. \*\**P* < 0.01.

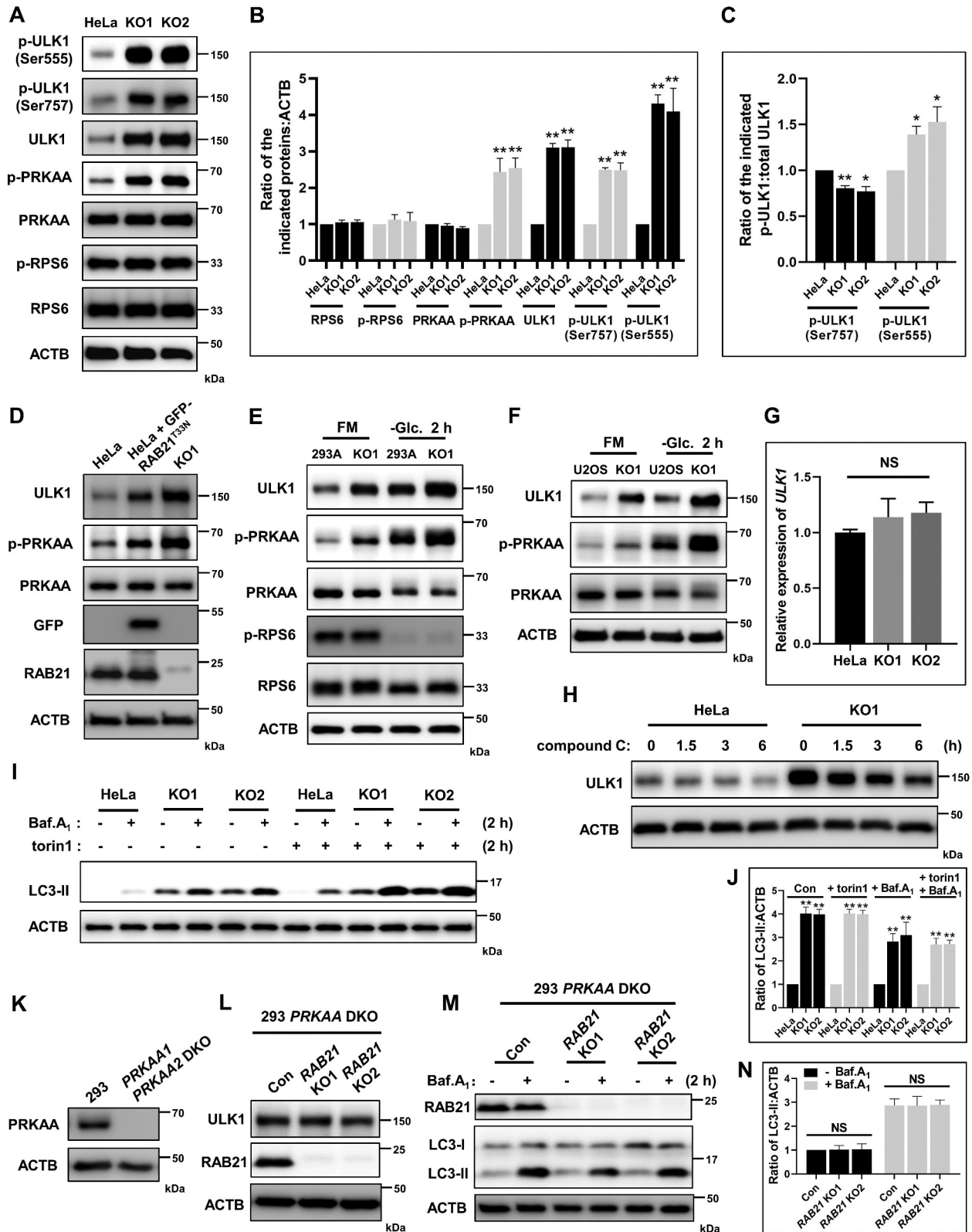


**Figure 3.** *RAB21* KO activates the AMPK-ULK1 pathway. (A-C) Immunoblot analysis of RPS6, p-RPS6, PRKAA, p-PRKAA, ULK1, p-ULK1 (Ser555), p-ULK1 (Ser757) and ACTB using whole-cell lysates of WT and *RAB21* KO HeLa cells. The quantitative results from three independent experiments are shown in B and C. (D) Immunoblot analysis of PRKAA, p-PRKAA, ULK1, GFP, RAB21 and ACTB in WT, GFP-RAB21<sup>T33N</sup>-expressing and *RAB21* KO HeLa cells. (E) WT and *RAB21* KO 293A cells were cultured in FM or -Glc. followed by immunoblot analysis with the indicated antibodies. (F) WT and *RAB21* KO U2OS cells were cultured in FM or -Glc. followed by immunoblot analysis with the indicated antibodies. (G) mRNA levels of ULK1 in WT and *RAB21* KO HeLa cells were determined by quantitative RT-PCR. (H-I) WT and *RAB21* KO HeLa cells were treated with 10  $\mu$ M compound C for the indicated time points and then lysed for immunoblot analysis of ULK1. (J) WT and *RAB21* KO HeLa cells were treated with Baf.A<sub>1</sub> (100 nM), torin1 (250 nM), or Baf.A<sub>1</sub> plus torin1 and then lysed for immunoblot analysis of LC3. The quantitative results from three independent experiments are shown in J. (K) WT and *PRKAA1 PRKAA2* double-KO (DKO) 293 cells were immunoblotted for PRKAA. (L) *PRKAA1 PRKAA2* DKO and *PRKAA1 PRKAA2* and *RAB21* triple KO (*RAB21* KO1, *RAB21* KO2) 293 cells were lysed for immunoblot analysis with the indicated antibodies. (M-N) the same cells as shown in L were cultured in the presence or absence of 100 nM Baf.A<sub>1</sub> and lysed for immunoblot analysis with the indicated antibodies. The quantitative results from three independent experiments are shown in N. The graphs express the mean  $\pm$  SEM. \* $P < 0.05$ ; \*\* $P < 0.01$ ; NS, not significant.

AMPK $\alpha$  phosphorylation (p-PRKAA, T172) (Figure 3A-F). AMPK inhibits MTORC1 activity by phosphorylating TSC2 and Raptor [30,31]. We hypothesized that the moderate and chronic activation of AMPK in *RAB21* KO cells might not be enough to inhibit MTORC1 activity or that the inhibition of MTORC1 activity was buffered by the increased autophagic flux that would produce additional nutrients to activate MTORC1. Indeed, glucose starvation induced acute activation of AMPK and efficiently inhibited MTORC1 activity in both WT and *RAB21* KO 293A cells (Figure 3E). We noted that *RAB21* KO increased ULK1 protein levels independent of *ULK1* transcription (Figure 3A-G), consistent with a previous report that AMPK regulates ULK1 protein stability [32]. We further confirmed that *RAB21* KO caused an increase in ULK1 protein levels downstream of AMPK by using the AMPK inhibitor compound C, which efficiently decreased ULK1 protein levels in KO cells (Figure 3H). Expressing GFP-*RAB21*<sup>T33N</sup> in WT cells also caused increases in p-PRKAA and ULK1 protein levels, further suggesting that *RAB21* regulates the AMPK-ULK1 pathway and autophagic flux (Figure 3D). It is worth noting that the phosphorylation of the AMPK substrate ULK1 (p-ULK1, Ser555) and the phosphorylation of the MTORC1 substrate ULK1 (p-ULK1, Ser757) were both elevated (Figure 3A-B), but when unified to total ULK1, the rate of p-ULK1 Ser555 was higher, while the rate of p-ULK1 Ser757 was lower in *RAB21* KO HeLa cells than in WT cells (Figure 3C), further indicating an activated AMPK pathway in *RAB21* KO cells.

To further evaluate whether *RAB21* KO cells have an intact MTORC1 pathway and a higher capacity for autophagic flux due to increased ULK1, we applied the MTORC1-specific inhibitor torin1 to inhibit MTORC1 activity and examined autophagic flux. The results showed that torin1 efficiently increased autophagic flux in both WT and KO cells, and KO cells exhibited significantly higher autophagic flux than WT cells in the presence of torin1 (Figure 3I-J).

To further confirm that *RAB21* KO increased ULK1 protein stability and autophagic flux through AMPK, *PRKAA1* *PRKAA2* double knockout (DKO) cells were generated via the CRISPR-Cas9 strategy (Figure 3K). Based on these DKO cells, *RAB21* was subsequently knocked out, and the results showed that *RAB21* KO had no overt influence on either ULK1 levels or autophagic flux (Figure 3L-N).

These results together indicate that *RAB21* regulates autophagic flux via the AMPK-ULK1 axis. The elevation of AMPK activity in *RAB21* KO cells may confer these cells more resistance to ferroptosis induced by Era., as AMPK inhibits ferroptosis by phosphorylating acetyl-CoA carboxylase and suppressing polyunsaturated fatty acid biosynthesis [33].

### ***RAB21* KO disrupts retrograde trafficking of SLC2A1 and affects glucose uptake**

Previous studies linked *RAB21* and its guanine nucleotide exchange factor ANKRD27/VARP to retromer [34,35], and given that *RAB21* is localized on early endosomes and regulates AMPK activity, we hypothesize that *RAB21* may regulate retrograde trafficking of SLC2A1, a ubiquitously expressed glucose transporter and well-defined retromer cargo [36,37].

To this end, immunostaining was performed to examine the cellular localization of SLC2A1 and the lysosomal marker LAMP1. The results showed that SLC2A1 signals were mainly enriched on the plasma membrane and some intracellular vesicles without overlap with LAMP1 in WT cells, while in *RAB21* KO cells, SLC2A1 signals were enriched on intracellular vesicles and showed significant overlap with LAMP1 (Figure 4A-B and Fig. S2). Furthermore, mis-sorting of SLC2A1 in *RAB21* KO cells was rescued by re-expressing GFP-*RAB21* (Figure 4C). We further performed a cell surface protein biotinylation experiment to measure SLC2A1 protein levels on the cell surface and found that *RAB21* KO cells had less SLC2A1 on the cell surface than WT cells, with unaltered total SLC2A1 protein levels (Figure 4D-E). These results suggest that *RAB21* regulates the retrograde trafficking of SLC2A1.

We next evaluated the efficiency of glucose uptake in *RAB21* KO cells by incorporating a fluorescent D-glucose analog, 2-NBDG, in the medium, which could be taken up by cells and measured by flow cytometry. The results showed that the fluorescence intensity in *RAB21* KO cells was much lower than that in WT cells, indicating inefficient glucose uptake (Figure 4F-G). The SLC2A1 inhibitor BAY-876 was used as a positive control, which efficiently reduced glucose uptake by WT cells (Figure 4F-G). We infer that inefficient glucose uptake by *RAB21* KO cells caused AMPK activation and thus increased autophagic flux, as the AMPK pathway is more sensitive to glucose than other nutrients.

We next examined whether *RAB21* affects retrograde transportation from endosomes to the TGN. Two typical cargos, WLS and IGF2R, were selected for examination. It has been reported that loss of function of VPS35 or VPS26 causes mis-sorting of WLS and IGF2R from the TGN to endolysosomes [15,35,38]. Our results indicated that *RAB21* KO did not overtly affect the cellular localization of WLS or IGF2R (Figure 5H-J).

### ***RAB21* KO affects the subcellular localization of retromer and WASH complexes and endosome morphology**

Retrograde trafficking of SLC2A1 from endosomes to the plasma membrane is mediated by the retromer complex, which comprises a core VPS35-VPS29-VPS26 trimer and associates with a range of proteins or protein complexes to sort cargos and generate endosomal tubular-vesicular carriers [10,11]. Silencing or mutating any member of the core retromer trimer, cargo receptor SNX27 or WASH complex causes mis-sorting of SLC2A1 to lysosomes [37,39]. Therefore, we first examined whether *RAB21* KO affected the stability of the core retromer complex and the interaction between the retromer complex and SNX27 or the WASH complex. To this end, we first constructed a *VPS35* KO HeLa cell line and re-expressed GFP-*VPS35* in these cells. *RAB21* was subsequently knocked out in these cells, and GFP-Trap was used for immunoprecipitation. The results showed that *RAB21* KO had no overt effect on the stability of the retromer core complex or the protein expression of VPS35, VPS26 or VPS29 (Figure 5A). The interaction between the retromer and the SLC2A1 retrograde receptor SNX27 or the guanine nucleotide



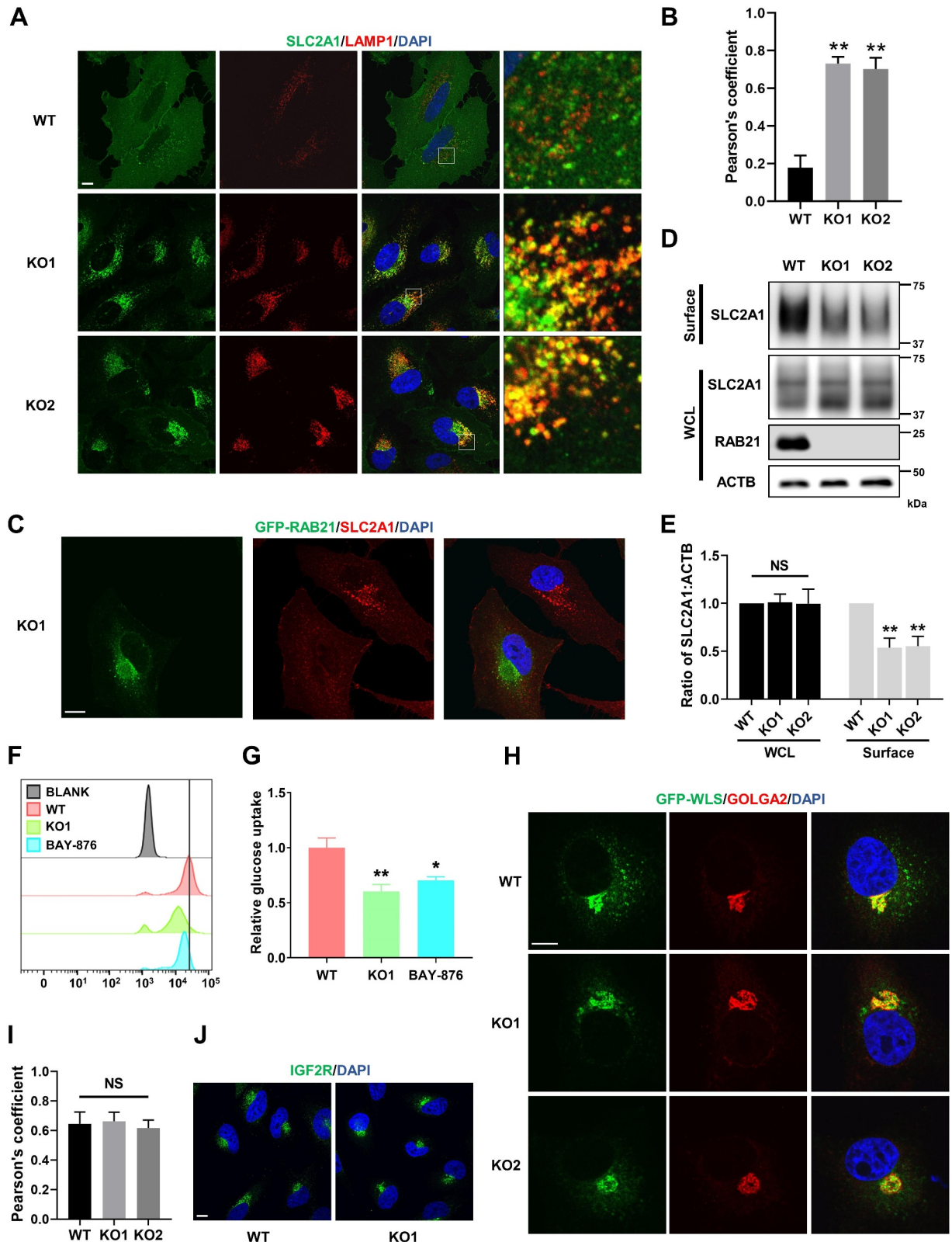


**Figure 4.** *RAB21* KO disrupts retrograde trafficking of SLC2A1 and affects glucose uptake. (A) WT and *RAB21* KO HeLa cells were immunostained for SLC2A1 (green) along with LAMP1 (red). (B) Colocalization of SLC2A1 with LAMP1 in a was analyzed by calculation of Pearson's coefficients ( $n > 25$  cells from three independent experiments). (C) *RAB21* KO re-expressing GFP-*RAB21* HeLa cells were mixed and seeded onto coverslips for SLC2A1 (red) immunostaining. (D-E) WT and *RAB21* KO HeLa cells were surface-biotinylated, followed by streptavidin isolation and immunoblot analysis. Surface, cell surface proteins. WCL, whole cell lysate. The quantitative results from three independent experiments are shown in E. (F-G) WT and *RAB21* KO HeLa cells were cultured with 100  $\mu$ M 2-NBDG for 4 h, and 2-NBDG uptake was measured by flow cytometry. WT HeLa cells pretreated with 10  $\mu$ M BAY-876 for 24 h were used as a positive control. The results from three independent experiments were statistically analyzed in G. (H-I) GFP-WLS was expressed in WT and *RAB21* KO HeLa cells. The colocalization of GFP-WLS with GOLGA2 was detected by immunostaining. The Pearson's coefficients ( $n > 20$  cells from three independent experiments) are shown in I. (J) the subcellular localizations of endogenous IGF2R in WT and *RAB21* KO HeLa cells were detected by immunostaining. Scale bars: 10  $\mu$ m. The graphs express the mean  $\pm$  SEM. \* $P < 0.05$ ; \*\* $P < 0.01$ ; NS, not significant.

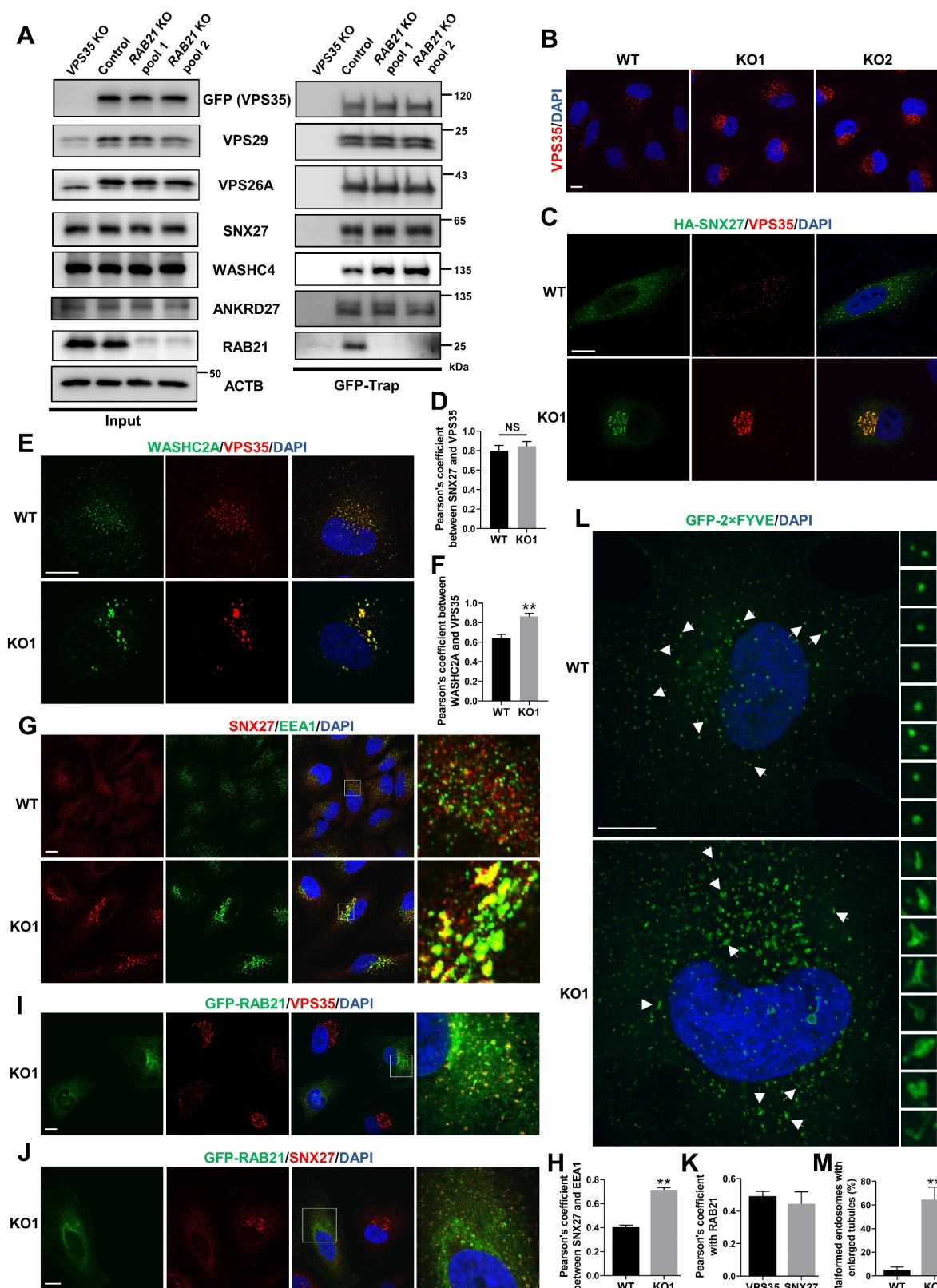


**Figure 5.** *RAB21* KO affects the subcellular localization of retromer and WASH and endosome morphology. (A) GFP-VPS35 was stably expressed in *VPS35* KO HeLa cells, and two *RAB21* KO cell pools were constructed on this basis. Endogenous VPS29, VPS26A, SNX27, WASHC4, ANKRD27 and RAB21 were coprecipitated by GFP-VPS35 in GFP-Trap assays. (B) WT and *RAB21* KO HeLa cells were immunostained for VPS35. (C-D) HA-SNX27-expressing WT and *RAB21* KO HeLa cells were immunostained for VPS35 along with HA. The Pearson's coefficients ( $n > 25$  cells from three independent experiments) are shown in D. (E-F) WT and *RAB21* KO HeLa cells were immunostained for VPS35 along with WASHC2A. The Pearson's coefficients ( $n > 25$  cells from three independent experiments) are shown in F. (G-H) WT and *RAB21* KO HeLa cells were immunostained for SNX27 along with EEA1. The Pearson's coefficients ( $n > 25$  cells from three independent experiments) are shown in H. (I-K) *RAB21* KO and *RAB21* KO re-expressing GFP-RAB21 HeLa cells were mixed and seeded onto coverslips for VPS35 or SNX27 immunostaining. The Pearson's coefficients ( $n > 20$  cells from three independent experiments) between VPS35 or SNX27 and RAB21 are shown in K. (L-M) GFP-2x FYVE was expressed in WT and *RAB21* KO HeLa cells and was observed for endosome morphology. The percentage of malformed endosomes with enlarged tubules was analyzed, and the quantitative results are shown in M ( $n > 30$  cells from three independent experiments). Scale bars: 10  $\mu$ m. The graphs express the mean  $\pm$  SEM. \*\* $P < 0.01$ ; NS, not significant.



exchange factor (GEF) of RAB21, ANKRD27, was unchanged, but the binding between the retromer complex and WASHC4/KIAA1033, a WASH complex component, was strengthened in *RAB21* KO cells (Figure 5A). Importantly, RAB21 was coimmunoprecipitated by VPS35 (Figure 5A), implying a functional correlation between RAB21 and SLC2A1 retrograde trafficking.

We next performed immunostaining to detect the endogenous protein localization of VPS35 and SNX27 in both WT and *RAB21* KO cells. The results showed that VPS35 exhibited a scattered puncta distribution in WT cells (Figure 5B). However, in *RAB21* KO cells, VPS35 puncta were enlarged in size and concentrated on one side of the nucleus around the Golgi network (Figure 5B and Fig. S3A). Similarly, *RAB21* KO caused mis-localization of SNX27 from a scattered puncta distribution pattern to more concentrated enlarged puncta surrounding the Golgi network (Fig. S3B), while the colocalization between VPS35 and SNX27 was unchanged in *RAB21* KO cells compared to WT cells (Figure 5C-D). We further performed immunostaining for WASHC2A/FAM21A, another component of the WASH complex, along with VPS35 and found that their colocalization was increased by *RAB21* KO (Figure 5E-F), consistent with the strengthened interaction between VPS35 and WASHC4.

*RAB21* KO also caused enlarged early endosomes in the perinuclear region and more SNX27 protein localized on early endosomes (Figure 5G-H). Re-expressing GFP-RAB21 in KO cells completely rescued the mis-localization of VPS35 and SNX27, suggesting a specific effect of *RAB21* KO (Figure 5I-J). We also observed significant colocalization between RAB21 and VPS35 or SNX27 (Figure 5I-K), further verifying the temporal-spatial correlation between retromer and RAB21.

To better illuminate the precise structure of endosomes, a GFP-fused 2×FYVE (GFP-2×FYVE) protein was expressed in both WT and *RAB21* KO HeLa cells. As shown in Figure 5L, most of the endosomes in WT cells presented as regular spheres, while in *RAB21* KO cells, the majority of the endosomes became irregular in shape, with enlarged tubules spreading around (Figure 5L-M).

Together, these results suggest that RAB21 may function downstream of the retromer and WASH complexes and may control the fission of tubular structures from endosomes. *RAB21* KO leads to the retention of retromer, SNX27 and the WASH complex on the enlarged endosomal tubules, thereby preventing retrograde trafficking from endosomes to the plasma membrane.

### ***RAB21* regulates lysosome activity**

The mCherry-GFP-LC3 reporter experiment indicated that *RAB21* KO cells may have more active lysosomes than WT cells (Figure 1K-L). We further applied LysoTracker Red, a fluorescent dye that stains acidic compartments (mainly lysosomes) in live cells, to label functional lysosomes in both WT and KO cells. The results showed that *RAB21* KO cells exhibited more intense fluorescent signals than WT cells, which could be rescued by re-expressing GFP-RAB21 (Figure 6A-B). Importantly, DQ-BSA, a molecular probe measuring the degradative activity of lysosomes, was applied to

both WT and *RAB21* KO cells for the indicated time points, and fluorescent signals were observed. As shown in Figure 6C-D, the fluorescent signals in *RAB21* KO cells appeared much faster and more intense than those in WT cells, suggesting that *RAB21* KO cells have more active lysosomes than WT cells. A previous study reported that *VPS35* KO causes defects in lysosome activity due to mis-sorting of IGF2R [35]. The fact that *RAB21* KO caused opposite effects on lysosome function compared to *VPS35* KO further suggests that *RAB21* KO has minimal interference on retrograde trafficking of IGF2R.

We noted that the fluorescence intensities of VPS35, SNX27, EEA1 and LAMP1 were all increased in *RAB21* KO cells compared to WT cells (Figures 4A, Figures 5B,G and 6E). We then performed immunoblotting to examine their total protein levels in both WT and *RAB21* KO cells and found no significant difference (Figure 6F-G), suggesting that the increased fluorescence intensities in *RAB21* KO cells are likely due to redistribution or concentration of these proteins on endosomes or lysosomes.

### ***SNX27* KO activates the AMPK-ULK1 axis and increases autophagic flux without affecting VPS35 localization and lysosome activity**

Based on our results on RAB21 and the fact that SNX27 controls retrograde transport of SLC2A1 from endosomes to the plasma membrane, we speculate that SNX27 may regulate autophagic flux via the AMPK-ULK1 axis. To examine this hypothesis and to compare the phenotypes between *SNX27* KO and *RAB21* KO cells, we generated *SNX27* KO HeLa cells via the CRISPR-Cas9 approach. We first confirmed that *SNX27* KO resulted in mis-sorting of SLC2A1 (Fig. S4A-B) and autophagic flux increase (Figure 7A), consistent with previous studies [37,40]. Importantly, p-PRKAA and ULK1 protein levels were increased in *SNX27* KO HeLa cells (Figure 7B), similar to those in *RAB21* KO cells, implying that *SNX27* regulates autophagy through the AMPK-ULK1 axis.

In contrast to *RAB21* KO, *SNX27* KO had no overt effect on the cellular localization of VPS35 or lysosome function, as shown by immunostaining of VPS35 and LysoTracker Red labeling of live cells (Figure 7C-D). Western blots revealed that the level of the mature active form of CTSB protein (heavy chain) in *RAB21* KO cells was significantly higher than that in WT and *SNX27* KO cells, although the levels of the CTSB protein precursor (pro-CTSB) were similar in all three types of cells (Figure 7E). These results indicated that RAB21 and SNX27 regulate retromer function via distinct mechanisms.

### ***RAB21* KO affects tumor growth**

Glucose is the most important energy source for the majority of cells, and cancer cells generally consume more glucose than normal cells, as cancer cells rely on glycolysis to generate ATP even under aerobic conditions (the Warburg effect) [41,42]. On the other hand, the glucose concentration in the cancer cell microenvironment is generally lower than that in normal

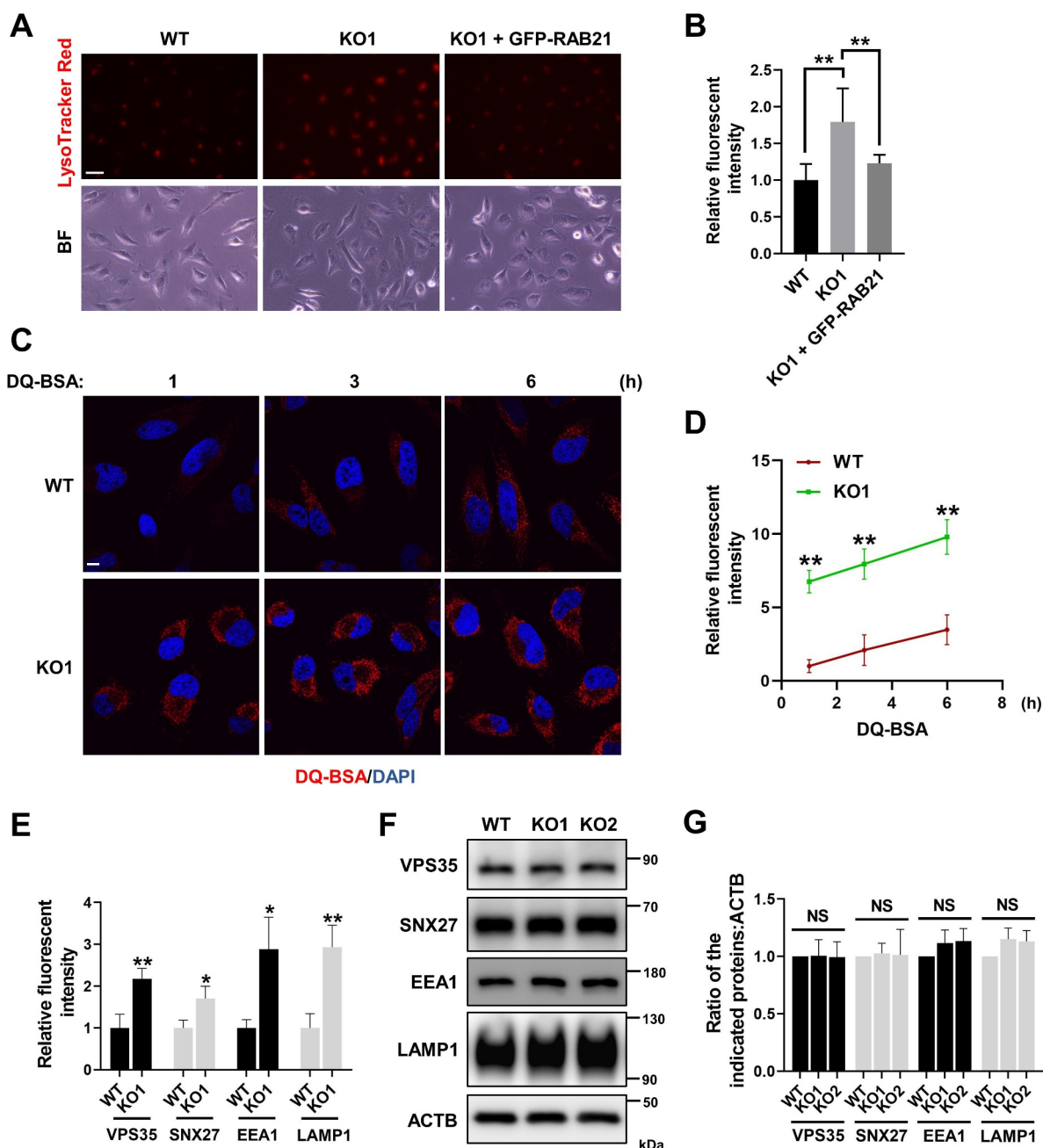


**Figure 6.** RAB21 regulates lysosome activity. (A–B) WT, *RAB21* KO and *RAB21* KO re-expressing GFP-RAB21 HeLa cells were labeled with LysoTracker Red. The quantitative results are shown in B ( $n > 60$  cells from three independent experiments). BF, bright field. Scale bar: 100  $\mu$ m. (C–D) the degradation capability of lysosomes in WT and *RAB21* KO HeLa cells was illuminated by DQ-BSA (red) at the indicated time points. The quantitative results are shown in D ( $n > 25$  cells from three independent experiments). Scale bar: 10  $\mu$ m. (E) Relative fluorescence intensity of VPS35, SNX27, EEA1 and LAMP1 in WT and *RAB21* KO HeLa cells ( $n > 20$  cells from three independent experiments). (F–G) Immunoblot analysis of VPS35, SNX27, EEA1, LAMP1 and ACTB using whole-cell lysates of WT and *RAB21* KO HeLa cells. The quantitative results from three independent experiments are shown in G. The graphs express the mean  $\pm$  SEM. \* $P < 0.05$ ; \*\* $P < 0.01$ ; NS, not significant.

tissues due to poor blood supply. Therefore, cancer cells often express high levels of glucose transporters such as SLC2A1, which has become a promising target for cancer therapy [14,43]. As RAB21 regulates retrograde transport of SLC2A1 and *RAB21* KO cells are more sensitive to energy stress, we speculate that RAB21 may play a critical role in cancer. We next utilized a cancer cell-derived xenograft model to examine this hypothesis. As cancer cells are heterogeneous, to avoid clonal variation, we constructed *RAB21* KO cell pools using HeLa cells via the CRISPR-Cas9 approach. Western blots

confirmed efficient knockout of *RAB21* and elevation of autophagic flux in both KO pools (Figure 8A). CCK-8 analysis revealed that *RAB21* KO significantly decreased cell proliferation under normal conditions (Figure 8B). To visualize the effect of *RAB21* KO on tumor growth in vivo, control and *RAB21* KO cells were subcutaneously injected into immunodeficient mice, and tumors were measured. The results showed that *RAB21* KO significantly affected tumor growth, as KO cells developed fewer and smaller tumors than control cells (Figure 8C–D and Fig. S5A).

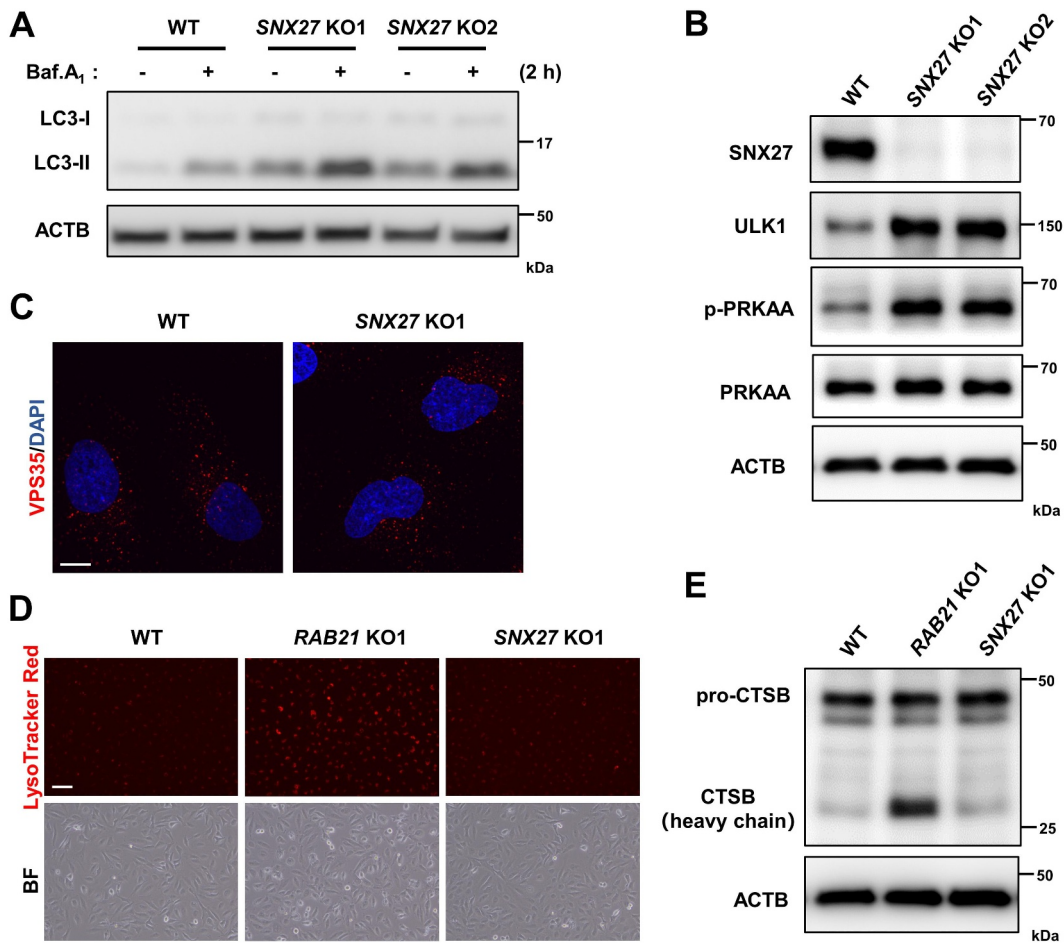


**Figure 7.** *SNX27* KO activates the AMPK-ULK1 axis and increases autophagic flux without affecting VPS35 localization and lysosomal activity. (A) WT and *SNX27* KO HeLa cells were cultured in FM with or without 100 nM Baf.A<sub>1</sub> and were lysed and immunoblotted for LC3. (B) Immunoblot analysis of ULK1, p-PRKAA, PRKAA, *SNX27* and ACTB in WT and *SNX27* KO HeLa cells. (C) WT and *SNX27* KO HeLa cells were immunostained for VPS35. Scale bar: 10  $\mu$ m. (D) lysosomes of WT, *RAB21* KO and *SNX27* KO HeLa cells were labeled with LysoTracker Red. Scale bar: 100  $\mu$ m. (E) Immunoblot analysis of CTSB in WT, *RAB21* KO and *SNX27* KO HeLa cells.

We further examined *RAB21* function in MDA-MB-231 cells, a triple-negative breast cancer cell line that is sensitive to glucose deprivation [43]. Western blots and CCK-8 analysis revealed that *RAB21* KO caused an increase in p-PRKAA, p-ULK1 (Ser555) and LC3-II and a decrease in cell proliferation (Figure 8E-F), but the levels of total ULK1 and p-ULK1 (Ser757) were unchanged. In vivo tumor xenograft assays indicated that *RAB21* KO cell-derived tumors were smaller in volume and weight than control tumors (Figure 8G-I). To further evaluate tumor growth, the largest three tumors of *RAB21* KO and the smallest three tumors of control, which were similar in size, were chosen for further analysis. We found that *RAB21* KO-derived tumors were hollow inside, while control tumors were solid inside (Fig. S5B). Furthermore, *RAB21* KO-derived tumors contained fewer proliferating cells than control tumors, as revealed by MKI67 immunohistochemistry analysis (Fig. S5B). As a validation, we further performed immunoblotting analysis of the largest four *RAB21* KO tumors and the smallest four control tumors. The results showed that the levels of

p-PRKAA, p-ULK1 (Ser555) and LC3-II were higher in *RAB21* KO tumors than in control tumors (Figure 8J-L), indicating the activation of the AMPK-ULK1 pathway in *RAB21* KO tumors. These results together suggest that *RAB21* confers tumor cells the ability to survive in a stressed microenvironment and thus plays critical roles in cancer.

## Discussion

Our current study uncovered critical roles of *RAB21* in controlling retrograde transport of SLC2A1 from endosomes to the plasma membrane and maintaining cellular energy homeostasis. In the absence of *RAB21*, SLC2A1 was mis-sorted to lysosomes, and glucose uptake was dampened, which further activated the AMPK-ULK1 pathway to increase autophagic flux (Figure 9). Our results also revealed that *RAB21* associates with the retromer complex on endosomes and controls endosomal tubule fission.



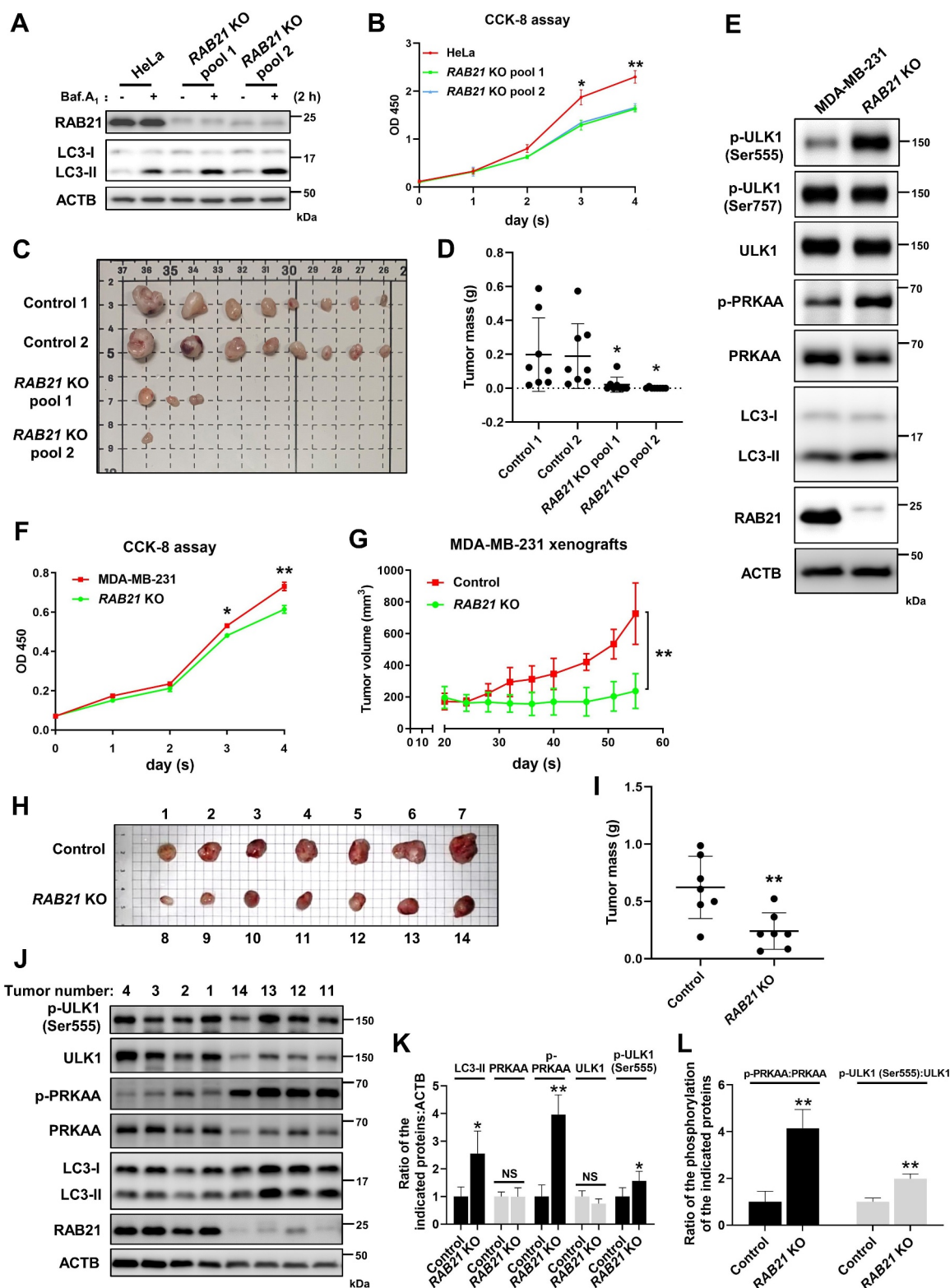


**Figure 8.** RAB21 KO affects tumor growth. (A) RAB21 KO HeLa cell pools were constructed via two distinct sgRNAs, and autophagic flux was examined. (B) a CCK-8 assay was performed at different time points to examine the effect of RAB21 KO on HeLa cell growth. (C) Images of xenograft tumors derived from HeLa cells. Scale bars: 10 mm. n = 8 mice per group. (D) Weights of xenograft tumors from C. n = 8 mice per group. (E) Immunoblot revealed that RAB21 KO caused elevations in p-ULK1 (Ser555), p-PRKAA and LC3-II in MDA-MB-231 cells. (F) a CCK-8 assay was performed at different time points to examine the effect of RAB21 KO on the growth of MDA-MB-231 cells. (G) Xenograft tumor growth in mice. The volumes of tumors burdened in nude mice receiving the MDA-MB-231 RAB21 KO cell pool or control cells were measured on different days after implantation. n = 7 mice per group. (H) Images of mouse xenograft tumors from G. Scale bars: 10 mm. n = 7 mice per group. (I) Weights of mouse xenograft tumors from H. n = 7 mice per group. (J-L) Immunoblot analysis of RAB21, LC3, PRKAA, p-PRKAA, ULK1, p-ULK1 (Ser555) and ACTB using the indicated tumors from H. The quantitative results are shown in K and L (n = 4). The graphs express the mean  $\pm$  SEM. \*P < 0.05; \*\*P < 0.01; NS, not significant.

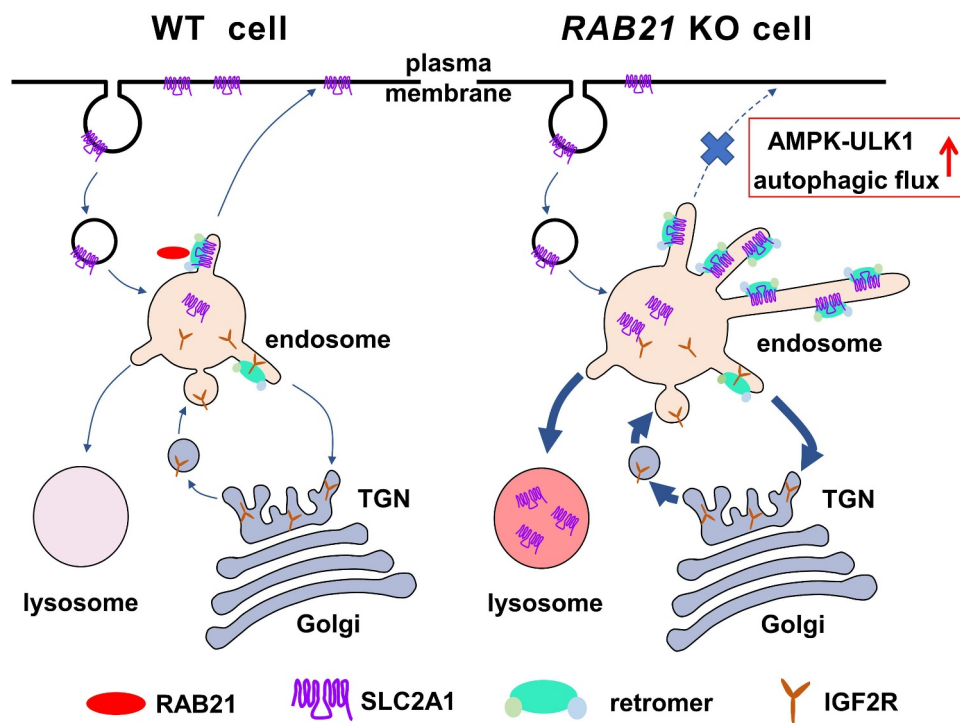


**Figure 9.** A graphic model for the roles of RAB21 in retromer-mediated cargo sorting. In WT cells, the retromer mediates the recycling of membrane proteins such as SLC2A1 from endosomes to the plasma membrane with the assistance of RAB21, ensuring efficient glucose uptake. The retromer is also in charge of the retrograde transport of receptor proteins such as IGF2R from endosomes to the TGN for continuous delivery of hydrolases to lysosomes and maintenance of lysosome function. RAB21 depletion prevents the dissociation of retromer-decorated tubules from endosomes, disrupts endosome to plasma membrane recycling of SLC2A1 and mis-sorts SLC2A1 to lysosomes for degradation, thereby affecting glucose uptake and activating the AMPK-ULK1 pathway and autophagic flux. Meanwhile, trafficking between endosomes and the TGN is likely strengthened, rendering IGF2R more efficient in delivering lysosomal hydrolases such as CTSB, thereby increasing lysosome activity.

Jean S. et al reported that RAB21 promotes autophagosome-lysosome fusion under starvation conditions and thus plays a positive role in autophagy [23]. They have used RNAi approach in their entire study, and the efficiency and potential off-target effect of the siRNAs could not be excluded. In contrast, in the current study, we utilized the CRISPR-Cas9 approach to knock out *RAB21* and convincingly showed that *RAB21* KO caused an increase in autophagic flux under both basal and starvation conditions in multiple cell lines (Figure 1). Furthermore, *RAB21* KO cells contained more autolysosomes than WT cells, as shown by the mCherry-GFP-LC3 reporter (Figure 1K-L), further suggesting that RAB21 inhibits, rather than promotes, autophagosome-lysosome fusion. Our results suggest that *RAB21* KO activates the AMPK-ULK1 axis to promote autophagic flux, as depletion of PRKAA1 and PRKAA2 completely abolished *RAB21* KO-induced ULK1 protein levels and autophagic flux increases (Figure 3K-N).

RAB21 was reported to associate with WASH and retromer complexes and regulate the retrograde trafficking of a subset of cargos but not SLC2A1 [24]. The main drawback of this study is that they used knockout cell pools in immunostaining experiments to observe single-cell behavior without confirming *RAB21* knockout in these cells. To obtain reliable results, we used single clones of *RAB21* KO cells for all immunostaining assays and analyzed multiple cells from different clones.

Our results undoubtedly showed that *RAB21* KO results in mis-sorting of SLC2A1 to lysosomes and reduction of SLC2A1 protein levels on the cell surface (Figure 4). Importantly, all the phenotypes caused by *RAB21* KO were successfully rescued by re-expressing GFP-RAB21.

SNX27 controls retromer-mediated recycling from endosomes to the plasma membrane by recognizing and binding to specific cargos, including SLC2A1 [37,44]. Yang Z. et al reported that knockout of *SNX27* enhanced autophagy, likely by impairing MTORC1 activity [40]. Our results indicated that *SNX27* KO resulted in activation of the AMPK-ULK1 pathway and an increase in autophagic flux (Figure 7), similar to the effects of *RAB21* KO, further supporting the existence of the SLC2A1-AMPK-ULK1 axis.

*RAB21* KO does not disrupt the retromer core complex or its association with SNX27, ANKRD27, or the WASH complex. However, it causes perinuclear enriched localization of VPS35, SNX27 and WASHC2A (Figure 5). All three proteins exhibit small punctum localization spreading in WT cells. As endosome fission is a critical step of retromer-mediated recycling [45], we speculate that RAB21 may regulate the fission of retromer-decorated endosomal tubules. Previous studies indicated that the WASH complex regulates endosome fission and retrograde trafficking and that *WASH* knockdown results in enlarged endosomes with long tubular structures [46,47]. *RAB21* KO results in similar morphological changes in

endosomes as *WASH* knockdown, and *RAB21* is associated with the retromer complex (Figure 5A), suggesting that *RAB21* may function downstream of the retromer complex to control endosomal tubule fission. Intriguingly, *RAB21* KO also resulted in increased co-localization and association between the retromer complex and the *WASH* complex (Figure 5A,5E,F). One possibility is that *RAB21* and the *WASH* complex function in parallel in regulating endosomal tubule fission, and *RAB21* KO-induced endosomal tubule fission defects increase binding between the retromer and *WASH* through compensatory feedback. It is also possible that *RAB21* and *WASH* compete in binding to the retromer complex. Furthermore, the retromer complex may activate *RAB21* by recruiting *ANKRD27* or other potential GEFs for *RAB21*. Activated *RAB21* may recruit effectors such as *APPL1* to regulate endosomal tubule fission. These subjects deserve further investigation.

Another phenotype caused by *RAB21* KO is the elevation of lysosome activity (Figure 6). The retromer complex was reported to control lysosome activity by regulating retrograde transport of *IGF2R*, a lysosomal hydrolase transporter, from the endosome to the Golgi network, and *VPS35* KO affects lysosome function [35]. Our results revealed that although *RAB21* KO does not overtly affect the cellular localization of *IGF2R*, the mature active form of *CTSB* is significantly increased in *RAB21* KO cells (Figure 7E). As *CTSB* is a typical cargo of *IGF2R*, we speculate that *RAB21* KO may enhance the transportation of *IGF2R* from endosomes to the TGN. Therefore, more hydrolases are delivered to endolysosomes. Furthermore, the enriched retromer-decorated endosomal structures in the perinuclear region surround the Golgi network in *RAB21* KO cells, which may facilitate more efficient trafficking between endosomes and the Golgi network (Figure 5).

Recent studies revealed a negative correlation between *RAB21* expression levels and the survival of cancer patients by analyzing cancer databases [48,49]. Our results further reveal that *RAB21* plays an oncogenic role in cancer in part by controlling the retrograde transport of *SLC2A1* and maintaining cellular energy homeostasis in cancer cells. Thus, *RAB21* may represent a potential metabolic target for cancer therapy.

## Materials and methods

### Antibodies and reagents

Antibodies used in the study: anti-LC3A/B (12741; 1:1000 for WB, 1:200 for IF), anti-GFP (2956; 1:1000 for WB), anti-EEA1 (3288; 1:200 for IF, 1:1000 for WB), rabbit anti-LAMP1 (9091; 1:200 for IF, 1:1000 for WB), mouse anti-LAMP1 (15665; 1:200 for IF), anti-ULK1 (8054; 1:1000 for WB), anti-p-ULK1 (Ser555) (5869; 1:1000 for WB), anti-p-ULK1 (Ser757) (6888; 1:1000 for WB), anti-PRKAA/AMPK $\alpha$  (5831; 1:1000 for WB), anti-p-PRKAA/AMPK $\alpha$  (2535; 1:1000 for WB), anti-RPS6 (2217; 1:1000 for WB), anti-p-RPS6 (4857; 1:1000 for WB), anti-HA (3724; 1:1000 for WB), anti-CTSB (31718; 1:1000 for WB) and anti-MKI67 (9449; 1:200 for IHC) were from Cell Signaling Technology; anti-*RAB21* (A12095; 1:1000 for WB),

anti-*ACTB* (AC026; 1:20000 for WB) and anti-*GOLGA2/GM130* (A5344; 1:200 for IF) were from ABclonal Technology; anti-*SLC2A1/GLUT1* (ab115730; 1:200 for IF, 1:4000 for WB), anti-*IGF2R* (ab124767; 1:200 for IF) and anti-*SNX27* (ab77799; 1:200 for IF, 1:1000 for WB) were from Abcam; anti-*VPS26A* (12804-1-AP; 1:1000 for WB), anti-*WASHC4/KIAA1033* (51101-1-AP; 1:1000 for WB) and anti-*ANKRD27/VARP* (24034-1-AP; 1:1000 for WB) was from Proteintech Group; anti-*VPS29* (sc-398874; 1:200 for WB) and anti-*VPS35* (sc-374372; 1:200 for WB, 1:100 for IF) were from Santa Cruz Biotechnology; anti-*WASHC2A/FAM21A* (57472; 1:200 for IF) was from Novus Biologicals; goat anti-rabbit IgG HRP (S0001; 1:10000) and goat anti-mouse IgG HRP (S0002; 1:10000) were from Affinity Biosciences; Alexa Fluor 488 donkey anti-rabbit IgG (H+L) (34206ES60; 1:400), Alexa Fluor 594 donkey anti-rabbit IgG (H+L) (34212ES60; 1:400), Alexa Fluor 488 donkey anti-mouse IgG (H+L) (34106ES60; 1:400) and Alexa Fluor 594 donkey anti-mouse IgG (H+L) (34112ES60; 1:400) were from Yeasen Biotechnology. Bafilomycin A<sub>1</sub> (HY-100,558), erastin (HY-15,763), compound C (HY-13418A) and ferrostatin-1 (HY-100,579) were purchased from MedChemExpress. Chloroquine (T0194), torin1 (T6045) and BAY-876 (T3713) were from Targetmol. Other reagents used in this study were DAPI (Solarbio, C0060), 2-NBGD (APEX-BIO, B6035), LysoTracker Red (Beyotime Biotechnology, C1046) and DQ-Red BSA (Thermo Fisher Scientific, D12051).

### DNA constructs

mCherry-GFP-LC3 was a kind gift from Qiming Sun [26]. pEGFP-C1-EGFP-*RAB21* WT and T33N were gifts from Arwyn T. Jones (Cardiff University, Cardiff, UK), and EGFP-*RAB21* WT and T33N were amplified by PCR and subcloned into the pLVX-puro vector (Clontech Laboratories, 632,164) using a Seamless Cloning Kit (CorYeabio Shanghai, KS218). The coding sequence of human *VPS35* was cloned into the pLVX-puro vector along with an *N*-terminal EGFP tag. The coding sequence of human *WLS* was cloned into the pLVX-puro vector along with a C-terminal EGFP tag. The coding sequence of human *SNX27* was cloned into the pLVX-puro vector along with an *N*-terminal HA tag. 2 $\times$ FYVE was generated by Tsingke Biotechnology Co., Ltd. and cloned into the pLVX-puro vector along with an *N*-terminal EGFP tag. All constructs were confirmed by DNA sequencing.

### Cell culture

HeLa (CRM-CCL-2), HEK293T (CRL-11,268), HEK293 (CRL-1573), U2OS (HTB-96) and MDA-MB-231 (CRM-HTB-26) cells from American Type Culture Collection (ATCC) and HEK293A (Procell, CL-0003) were cultured in high-glucose Dulbecco's modified Eagle's medium (DMEM) supplemented with 10% fetal bovine serum (BioChannel Biological Technology Co., Ltd., BC-SE-FBS07), 2 mM L-glutamine, 100 U/ml penicillin and 100  $\mu$ g/ml streptomycin at 37°C in a 5% CO<sub>2</sub> humidified incubator.



### Generation of CRISPR-Cas9 knockout cell lines

Human *RAB21* guide sequences (CTGCGTGG GGAAGACGTCGC; AGCGACGGGATGGCTCGGC; CAGCACCACCTTGAACGAGT), human *VPS35* guide sequence (GTTTGCTAAAGGAAGGAAAG), human *SNX27* guide sequences (GAACCACGTGAATGTTGAGG; TCGCCCCCTCAACATTCACG), human *PRKAA1* guide sequences (GAAGATTCGGAGCCTTGATG; TCCTGTTAC AGATTGTATGC) and human *PRKAA2* guide sequences (GAAACCAGAGAATGTCCTGT; ACGTTATTTAAG AAGATCCG) were ligated into the lentiCRISPR v2 plasmid (Addgene, 52961; deposited by Feng Zhang [50]) using the BsmBI site. For monoclonal knockout cell lines, the indicated cells were transfected with plasmid DNA using Liposomal Transfection Reagent (Yeasen Biotechnology, 40802ES03) according to the manufacturer's instructions and then selected using 1 µg/ml puromycin. Two days later, the cells were trypsinized (Basal Media, S310JV) and cloned by limited dilution. Clonal lines were isolated and analyzed by immunoblotting. For knockout cell pools, plasmid DNA was cotransfected with the lentiviral packaging vectors psPAX2 (Addgene, 12260; deposited by Didier Trono) and pMD2.G (Addgene, 12259; deposited by Didier Trono) into HEK293T cells. Lentiviral particles were collected 48 h after transfection. The indicated cells were infected with the collected lentiviral particles for 24 h, followed by selection using 1 µg/ml puromycin.

### Determination of cell death

Cell death was quantified under normal or nutrient starvation conditions using an ANXA5-FITC/PI detection kit (Solarbio, CA1020) according to the manufacturer's protocol. In brief, cells were washed in cold PBS (Basal Media, B210 KJ), resuspended in 1× binding buffer in the presence of ANXA5-FITC or PI and incubated at room temperature for 15 min in the dark. Analysis by flow cytometry was performed within 1 h.

### Immunoprecipitation and western blot

Cell pellets were homogenized in lysis buffer containing 20 mM Tris-HCl, 150 mM NaCl, 0.75% NP-40 (Solarbio, N8030), 1 mM NaF, protease cocktail (Targetmol, C0001), and phosphatase cocktail (Targetmol, C0002), pH 7.4, and incubated on ice for 30 min. The cell lysate was cleared by centrifugation at 21,130 × g for 15 min. The supernatant was incubated with antibody-conjugated beads and rotated for 12 h at 4°C. After incubation, the beads were washed 5 times with the same lysis buffer. Western blotting was performed following standard procedures.

### Immunofluorescence

Cells were grown on coverslips (NEST Biotechnology, 801,010) overnight, fixed in 4% paraformaldehyde (Sangon Biotech, E672002) in PBS for 20 min at room temperature and permeabilized with 0.1% Triton X-100 (Solarbio, T8200) in PBS for 20 min. Following permeabilization, cells were treated with block buffer (5% normal donkey serum [Yeasen Biotechnology,

36116ES03], 0.1% Tween-20 [Yeasen Biotechnology, 60305ES76] in PBS) for 1 h at room temperature. Cells were incubated with primary antibodies diluted in blocking buffer overnight at 4°C. Cells were washed three times with PBS, each for 10 min, followed by incubation with Alexa Fluor-conjugated secondary antibody (Yeasen Biotechnology, 34106ES60; 34112ES60; 34206ES60; 34212ES60) in block buffer for 1 h at room temperature. Finally, the cells were washed three times with PBS again and stained with DAPI (1 µg/ml). Slides were examined by using a laser scanning confocal microscope (Olympus FV3000). In each independent experiment, pictures for fluorescence intensity or puncta number analysis were taken, processed and presented under the same conditions among cells.

### Surface SLC2A1 biotinylation assay

Cells were seeded in 6-well plates (Jet Biofil, TCP010006). EZ-linked sulfo-NHS-SS-biotin (Thermo Fisher Scientific, A39258) was dissolved in PBS containing Ca<sup>2+</sup> and Mg<sup>2+</sup> (Basal Media, B220 KJ) at a concentration of 0.5 mg/ml. The cells were washed twice with cold PBS, and EZlink sulfo-NHS-SS-biotin was added for 30 min at 4°C. After incubation, the cells were washed with cold PBS containing 50 mM Tris-HCl, pH 7.4, six times and lysed. Biotinylated proteins were captured by incubating lysates with streptavidin ultralink resin (Thermo Fisher Scientific, 29,200) overnight. The captured proteins were recovered by mixing the beads with SDS loading buffer containing 10% 2-mercaptoethanol at room temperature for 2 h. The biotinylated proteins were resolved by SDS-PAGE and immunoblotted for SLC2A1.

### Glucose uptake assay

To measure glucose uptake, cells were seeded in 6-well plates. Culture medium was then removed from each well and replaced with 1 ml of fresh culture medium containing 100 µM fluorescent 2-NBDG (APEX-BIO, B6035). The cells were incubated at 37°C for 4 h. The cells were then washed twice with cold PBS and collected for flow cytometry analysis.

### Quantitative reverse transcription PCR (qRT-PCR)

RNA was extracted using an RNA Isolation Kit (Vazyme Biotech Co., Ltd, RC101), and cDNA was obtained using an RT Reagent Kit (CorYeabio Shanghai, KS202). qRT-PCR was performed with SYBR Green PCR Master Mix (CorYeabio Shanghai, KS203) using a CFX Connect Real-Time PCR Detection System (BIO-RAD). Experiments were performed using three independent RNAs. The qRT-PCR results were normalized to GAPDH and calculated following the 2<sup>-ΔΔCt</sup> method. The following sequences of primers were used: GAPDH-F: 5'-ACAACCTTGGTATCGTGAAGG-3'; GAPDH-R: 5'-GCCATCACGCCACAGTTTC-3'; ULK1-F: 5'-GGCAAGTTCGAGTTCTCCCG-3'; ULK1-R: 5'-CGACCTCCAAATCGTGCTTCT-3'.

### CCK-8 assay

To evaluate cell proliferation, a Cell Counting Kit-8 assay (Abbkine, Wuhan, China, BMU106-CN) was used according to the manufacturer's instructions. In brief, cells were plated in 96-well plates in quintuplicate at a concentration of 1000 cells per well. At the indicated time points, 10  $\mu$ l of CCK-8 solution was added, and the plate was returned to the incubator for another 1 h. Then, the OD450 of each well was recorded by a microplate reader.

### In vivo xenograft model

All animal procedures and experiments were approved by the Animal Care Committee of Huazhong University of Science and Technology and conducted according to the guidelines of the committee. Control and *RAB21* KO cell pools of HeLa and MDA-MB-231 were injected into female BALB/c nude mice subcutaneously at a concentration of  $5 \times 10^6$  cells per mouse. Tumor volume was recorded every 4 days after injection, and mice were killed before the largest tumor volume reached 1000 mm<sup>3</sup>. At the end of the experiment, the tumor weight was measured, and an immunohistochemistry assay of the tumor tissue was performed.

### Immunohistochemistry staining

Tissue sections were fixed in 10% neutral buffered formalin (Sangon Biotech, E672001) and embedded in paraffin. Tissue sections were routinely stained with hematoxylin and eosin (H&E). For immunohistochemistry staining, paraffin sections at 5  $\mu$ m thickness were dried in a 60°C oven for 2 h before staining. Immunohistochemistry (IHC) was performed using an IHC Kit (Solarbio, SP0021) according to the manufacturer's instructions. Antigen retrieval was performed by incubating the sections in boiling sodium citrate (10 mM, pH 6.0) followed by incubation with the indicated primary antibody overnight at 4°C. Antibody binding was detected by the IHC Kit. The slides were counterstained with Harris hematoxylin, dehydrated in graded alcohol, cleared in xylene and coverslipped in neutral balsam.

### Statistics

Two-tailed t tests (Microsoft Excel) were used to determine significance between two groups, and one-way ANOVA with post hoc analyses (GraphPad Prism 8) was used for multiple groups. All data representative of three independent experiments are presented as the mean  $\pm$  SEM. \* $P < 0.05$ ; \*\* $P < 0.01$ ; NS, not significant. Fluorescence intensity, puncta number and Pearson's correlation coefficients were calculated using ImageJ software (1.53n). For fluorescence intensity, each cell was selected and measured independently for the mean gray value. For puncta number, each cell was selected and measured independently for particle analysis. For Pearson's correlation coefficients, Colocalization Finder was used as a plug-in.

### Acknowledgments

We thank Qiming Sun at Zhejiang University, Yueguang Rong at Huazhong University of Science and Technology, Jiahong Lu at University of Macau, Yilei Zhang at Xi'an Jiaotong University, and Da Jia at Sichuan University for reagents and comments.

### Disclosure statement

No potential conflict of interest was reported by the author(s).

### Funding

The work was supported by the Fundamental Research Funds for the Central Universities [HUST2021GCRC033].

### Data availability statement

All data are contained within the manuscript.

### ORCID

Xinjun Zhang  <http://orcid.org/0000-0003-2409-4104>

### References

- [1] Zaffagnini G, Martens S. Mechanisms of selective autophagy. *J Mol Biol.* 2016 May 8;428(9 Pt A):1714–1724. DOI:10.1016/j.jmb.2016.02.004
- [2] Boya P, Reggiori F, Codogno P Emerging regulation and functions of autophagy. *Nat Cell Biol.* 2013 Jul;15(7):713–720.
- [3] Klionsky DJ, Abdelmohsen K, Abe A, et al. Guidelines for the use and interpretation of assays for monitoring autophagy (3rd edition). *Autophagy.* 2016;12(1):1–222.
- [4] Alers S, Loffler AS, Wesselborg S, et al. Role of AMPK-mTOR-Ulk1/2 in the regulation of autophagy: cross talk, shortcuts, and feedbacks. *Mol Cell Biol.* 2012 Jan;32(1):2–11. DOI:10.1128/MCB.06159-11
- [5] Hardie DG, Ross FA, Hawley SA. AMPK: a nutrient and energy sensor that maintains energy homeostasis. *Nat Rev Mol Cell Biol.* 2012 Mar 22;13(4):251–262. DOI:10.1038/nrm3311
- [6] Inoki K, Kim J, Guan KL AMPK and mTOR in cellular energy homeostasis and drug targets. *Annu Rev Pharmacol Toxicol.* 2012;52:381–400.
- [7] Laplante M, Sabatini DM. mTOR signaling in growth control and disease. *Cell.* 2012 Apr 13;149(2):274–293. DOI:10.1016/j.cell.2012.03.017
- [8] Kim J, Kundu M, Viollet B, et al. AMPK and mTOR regulate autophagy through direct phosphorylation of Ulk1. *Nat Cell Biol.* 2011 Feb;13(2):132–141. DOI:10.1038/ncb2152
- [9] Egan DF, Shackelford DB, Mihaylova MM, et al. Phosphorylation of ULK1 (hATG1) by AMP-activated protein kinase connects energy sensing to mitophagy. *Science.* 2011 Jan 28;331(6016):456–461. DOI:10.1126/science.1196371
- [10] Cullen PJ, Steinberg F To degrade or not to degrade: mechanisms and significance of endocytic recycling. *Nat Rev Mol Cell Biol.* 2018 Nov;19(11):679–696.
- [11] Chen KE, Healy MD, Collins BM Towards a molecular understanding of endosomal trafficking by retromer and retriever. *Traffic.* 2019 Jul;20(7):465–478.
- [12] Tu Y, Seaman MNJ Navigating the controversies of retromer-mediated endosomal protein sorting. *Front Cell Dev Biol.* 2021;9:658741.
- [13] Bonifacino JS, Hurley JH Retromer. *Curr Opin Cell Biol.* 2008 Aug;20(4):427–436.

- [14] Pliszka M, Szablewski L. Glucose transporters as a target for anticancer therapy. *Cancers (Basel)*. 2021 Aug 20;13(16):3390. DOI:10.3390/cancers13164184
- [15] Arighi CN, Hartnell LM, Aguilar RC, et al. Role of the mammalian retromer in sorting of the cation-independent mannose 6-phosphate receptor. *J Cell Biol*. 2004 Apr;165(1):123–133. DOI:10.1083/jcb.200312055
- [16] Zerial M, McBride H Rab proteins as membrane organizers. *Nat Rev Mol Cell Biol*. 2001 Feb;2(2):107–117.
- [17] Simpson JC, Griffiths G, Wessling-Resnick M, et al. A role for the small GTPase Rab21 in the early endocytic pathway. *J Cell Sci*. 2004 Dec 15;117(Pt 26):6297–6311. DOI:10.1242/jcs.01560
- [18] Yang X, Zhang Y, Li S, et al. Rab21 attenuates EGF-mediated MAPK signaling through enhancing EGFR internalization and degradation. *Biochem Biophys Res Commun*. 2012 May 18;421(4):651–657. DOI:10.1016/j.bbrc.2012.04.049
- [19] Zhang X, He X, Fu XY, et al. Varp is a Rab21 guanine nucleotide exchange factor and regulates endosome dynamics. *J Cell Sci*. 2006 Mar 15;119(Pt 6):1053–1062. DOI:10.1242/jcs.02810
- [20] Moreno-Layseca P, Jantti NZ, Godbole R, et al. Cargo-Specific recruitment in clathrin- and dynamin-independent endocytosis. *Nat Cell Biol*. 2021 Oct;23(10):1073–1084. DOI:10.1038/s41556-021-00767-x
- [21] Pellinen T, Arjonen A, Vuoriluoto K, et al. Small GTPase Rab21 regulates cell adhesion and controls endosomal traffic of beta1-integrins. *J Cell Biol*. 2006 Jun 5;173(5):767–780. DOI:10.1083/jcb.200509019
- [22] Pellinen T, Tuomi S, Arjonen A, et al. Integrin trafficking regulated by Rab21 is necessary for cytokinesis. *Dev Cell*. 2008 Sep;15(3):371–385. DOI:10.1016/j.devcel.2008.08.001
- [23] Jean S, Cox S, Nassari S, et al. Starvation-Induced MTMR13 and RAB21 activity regulates VAMP8 to promote autophagosome-lysosome fusion. *EMBO Rep*. 2015 Mar;16(3):297–311. DOI:10.15252/embr.201439464
- [24] Del Olmo T, Lauzier A, Normandin C, et al. APEX2-Mediated RAB proximity labeling identifies a role for RAB21 in clathrin-independent cargo sorting. *EMBO Rep*. 2019 Feb;20(2). DOI:10.15252/embr.201847192
- [25] Mizushima N, Yoshimori T How to interpret LC3 immunoblotting. *Autophagy*. 2007 Nov-Dec;3(6):542–545.
- [26] Cheng X, Ma X, Ding X, et al. Pacer mediates the function of Class III PI3K and HOPS complexes in autophagosome maturation by engaging Stx17. *Mol Cell*. 2017 Mar 16;65(6):1029–1043 e5. DOI:10.1016/j.molcel.2017.02.010
- [27] Gao M, Monian P, Pan Q, et al. Ferroptosis is an autophagic cell death process. *Cell Res*. 2016 Sep;26(9):1021–1032. DOI:10.1038/cr.2016.95
- [28] Hou W, Xie Y, Song X, et al. Autophagy promotes ferroptosis by degradation of ferritin. *Autophagy*. 2016 Aug 2;12(8):1425–1428. DOI:10.1080/15548627.2016.1187366
- [29] Zhou B, Liu J, Kang R, et al. Ferroptosis is a type of autophagy-dependent cell death. *Semin Cancer Biol*. 2020 Nov;66:89–100.
- [30] Gwinn DM, Shackelford DB, Egan DF, et al. AMPK phosphorylation of raptor mediates a metabolic checkpoint. *Mol Cell*. 2008 Apr 25;30(2):214–226. DOI:10.1016/j.molcel.2008.03.003
- [31] Inoki K, Zhu T, Guan KL. TSC2 mediates cellular energy response to control cell growth and survival. *Cell*. 2003 Nov 26;115(5):577–590. DOI:10.1016/S0092-8674(03)00929-2
- [32] Chung SJ, Nagaraju GP, Nagalingam A, et al. Adipoq/adiponectin induces cytotoxic autophagy in breast cancer cells through STK11/LKB1-mediated activation of the AMPK-ULK1 axis. *Autophagy*. 2017 Aug 3;13(8):1386–1403. DOI:10.1080/15548627.2017.1332565
- [33] Lee H, Zandkarimi F, Zhang Y, et al. Energy-Stress-Mediated AMPK activation inhibits ferroptosis. *Nat Cell Biol*. 2020 Feb;22(2):225–234. DOI:10.1038/s41556-020-0461-8
- [34] Hesketh GG, Perez-Dorado I, Jackson LP, et al. VARP is recruited on to endosomes by direct interaction with retromer, where together they function in export to the cell surface. *Dev Cell*. 2014 Jun 9;29(5):591–606. DOI:10.1016/j.devcel.2014.04.010
- [35] Cui Y, Carosi JM, Yang Z, et al. Retromer has a selective function in cargo sorting via endosome transport carriers. *J Cell Biol*. 2019 Feb 4;218(2):615–631. DOI:10.1083/jcb.201806153
- [36] Mueckler M, Thorens B The SLC2 (GLUT) family of membrane transporters. *Mol Aspects Med*. 2013 Apr-Jun;34(2–3):121–138.
- [37] Steinberg F, Gallon M, Winfield M, et al. A global analysis of SNX27-retromer assembly and cargo specificity reveals a function in glucose and metal ion transport (vol 15, pg 461, 2013). *Nat Cell Biol*. 2013 Jun;15(6):712. DOI:10.1038/ncb2780
- [38] Franch-Marro X, Wendler F, Guidato S, et al. Wingless secretion requires endosome-to-Golgi retrieval of Wntless/Evi/Sprinter by the retromer complex. *Nat Cell Biol*. 2008 Feb;10(2):170–177. DOI:10.1038/ncb1678
- [39] Jimenez-Organ A, Kvainickas A, Nagele H, et al. Control of RAB7 activity and localization through the retromer-TBC1D5 complex enables RAB7-dependent mitophagy. *Embo J*. 2018 Jan 17;37(2):235–254. DOI:10.15252/emboj.201797128
- [40] Yang Z, Follett J, Kerr MC, et al. Sorting nexin 27 (SNX27) regulates the trafficking and activity of the glutamine transporter ASCT2. *J Biol Chem*. 2018 May 4;293(18):6802–6811. DOI:10.1074/jbc.RA117.000735
- [41] Cairns RA, Harris IS, Mak TW Regulation of cancer cell metabolism. *Nat Rev Cancer*. 2011 Feb;11(2):85–95.
- [42] Hanahan D, Weinberg RA. Hallmarks of cancer: The next generation. *Cell*. 2011 Mar 4;144(5):646–674. DOI:10.1016/j.cell.2011.02.013
- [43] Barbosa AM, Martel F. Targeting glucose transporters for breast cancer therapy: the effect of natural and synthetic compounds. *Cancers (Basel)*. 2020 Jan 8;12(1):121. DOI:10.3390/cancers12010154
- [44] Temkin P, Lauffer B, Jager S, et al. SNX27 mediates retromer tubule entry and endosome-to-plasma membrane trafficking of signalling receptors. *Nat Cell Biol*. 2011 Jun;13(6):715–721. DOI:10.1038/ncb2252
- [45] Gautreau A, Oguievetskaia K, Ungermann C. Function and regulation of the endosomal fusion and fission machineries. *Cold Spring Harb Perspect Biol*. 2014 Mar 1;6(3):a016832. DOI:10.1101/cshperspect.a016832
- [46] Derivery E, Sousa C, Gautier JJ, et al. The Arp2/3 activator WASH controls the fission of endosomes through a large multiprotein complex. *Dev Cell*. 2009 Nov;17(5):712–723. DOI:10.1016/j.devcel.2009.09.010
- [47] Gomez TS, Billadeau DD A FAM21-containing WASH complex regulates retromer-dependent sorting. *Dev Cell*. 2009 Nov;17(5):699–711.
- [48] Anand S, Khan MA, Khushman M, et al. Comprehensive analysis of expression, clinicopathological association and potential prognostic significance of RABs in pancreatic cancer. *Int J Mol Sci*. 2020 Aug 4;21(15):5580. DOI:10.3390/ijms21155580
- [49] Choe EK, Lee S, Kim SY, et al. Prognostic effect of inflammatory genes on Stage I–III colorectal cancer—Integrative analysis of TCGA data. *Cancers (Basel)*. 2021 Feb 11;13(4):751. DOI:10.3390/cancers13040751
- [50] Sanjana NE, Shalem O, Zhang F Improved vectors and genome-wide libraries for CRISPR screening. *Nat Methods*. 2014 Aug;11(8):783–784.